Japanese Journal of Applied Physics **62**, 066502 (2023) **REGULAR PAPER**
https://doi.org/10.35848/1347-4065/acd3cb

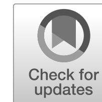

Monte Carlo characterization of Si ring modulator PAM-4 eye diagram performance

Youngkwan Jo[1], Yongjin Ji[1], Minkyu Kim[2], Stefan Lischke[3], Christian Mai[3], Lars Zimmermann[3,4], and Woo-Young Choi[1*]

[1]*Department of Electrical and Electronic Engineering, Yonsei University, Seoul, 03722, Republic of Korea*
[2]*Formerly in Department of Electrical and Electronic Engineering, Yonsei University, now at IMEC, 3001 Leuven, Belgium*
[3]*IHP—Leibniz-Institut für innovative Mikroelektronik, 15236 Frankfurt (O.), Germany*
[4]*Technische Universität Berlin, Einsteinufer 25, 10587 Berlin, Germany*

*E-mail: wchoi@yonsei.ac.kr

Received October 20, 2022; revised April 25, 2023; accepted May 9, 2023; published online June 9, 2023

The eye diagram performance of the Si ring modulator (RM) is Monte Carlo characterized with the RM equivalent circuit model. Inter-die statistical distributions of Si-RM model parameters are determined from simple RM optical transmission and electrical reflection coefficient measurement, and the correlated model parameter sets are randomly generated for Monte Carlo simulation of 40-Gbps 4-level pulse AM (PAM-4) eye diagrams within simulation program with IC emphasis. From the resulting Monte Carlo simulated eye diagrams, the yield for the Si RMs that satisfy optical modulation amplitude and the ratio of level mismatch requirements can be corroborated with measurement. With these, the eye diagrams of Si electronic-photonic integrated PAM-4 transmitters with RMs and driver electronics are Monte Carlo characterized. This approach allows the extension of the standard Si IC characterization technique to the electronic-photonic ICs and can produce better-performing solutions with better yields in the design stage. © 2023 The Japan Society of Applied Physics

1. Introduction

Si photonics, with its capacity for cost-effective fabrication of large-scale photonic ICs (PIC) can provide high-performance solutions for many important applications such as data-center interconnects,[1] sensors,[2,3] microwave photonics,[4,5] and newly emerging quantum[6,7] and neuromorphic computing.[8,9] For these applications, such process variations as those in silicon-on-insulator (SOI) thickness, waveguide width, and doping concentrations can greatly affect the performance and the yield of the resulting Si PICs,[10–12] and, consequently, their statistical distribution and its influence on the PIC performance must be carefully investigated. In the case of Si IC technology, the performance of the target IC can be very precisely predicted in the design stage by various corner simulations[13] and Monte Carlo analysis techniques[14] using the statistical data provided by the IC manufacturer. Such a statistics-based approach should be also employed for Si PIC technology so that design reliability and fabrication productivity can be further improved than is currently possible, and more cost-effective and higher-performance Si photonics solutions for various applications can be achieved.

There are some previous research results for Si photonics in this direction. The influence of waveguide geometry variation such as SOI thickness and waveguide linewidth was investigated.[10–12] Layout-aware behavioral simulations with the wafer-scale information on spatially correlated layout dependency were carried out.[15,16] However, there is a very limited number of publications[17,18] on the statistical investigation of active Si photonic devices such as modulators, although process variation can have significant influences on the Si active device characteristics and, consequently, the total performance of Si PICs.

We apply the Monte Carlo characterization technique to the depletion-type Si ring modulators (RMs). The Si RM has the advantages of a small footprint, high modulation bandwidth, and high energy efficiency,[19,20] but it is a very sensitive device, and its characteristics are vulnerable to the statistical variation in the fabrication process such as doping concentration, waveguide width, and the coupling gap of the directional coupler. As the application of the Si RM is being extended from very high-speed data center interconnect applications to co-packaged optical I/Os,[21] the statistical characterization of Si RM performance is of great importance. However, previously published reports regarding the statistical studies on the Si RM are mostly focused on the resonator characteristics of RM[10–12,15,17] while the modulator characteristics of RMs such as electro-optic efficiency, bandwidth and output Optical Modulation Amplitude (OMA) are important. This is due to the fact that it is hard to correlate the variation of device geometry and fabrication conditions of RMs to their modulation performance variation. In this paper, the eye diagram performance for 40-Gbps 4-level pulse AM (PAM-4) modulation of depletion-type Si RMs is statistically characterized with the newly proposed parametric Monte Carlo approach. With the inter-die statistics of key model parameters acquired from the measurements of fabricated Si RMs, correlated model parameter sets are randomly generated. With the resulting model parameters, a Monte Carlo simulation of PAM-4 eye diagrams is carried out using the previously reported equivalent circuit for the Si RM in the simulation program with IC emphasis (SPICE), the standard IC design simulation tool. From the Monte Carlo simulated eye diagrams, the 2-D histogram for the PAM-4 OMA and the Ratio of Level Mismatch (RLM) is produced. These results are corroborated by measurement. In addition, the approach can be expanded to the yield estimation of Si electronic-photonic ICs (EPICs) PAM-4 transmitters based on RMs. The EPICs integrate Si electronic circuits with Si photonic devices on a monolithic chip, which improves overall performance by eliminating chip-to-chip interconnections between electronic and photonic ICs and bringing photonics as close to electronics as possible. By using the equivalent circuit of RMs, the yield of any EPIC transmitter containing RMs can be efficiently estimated in the design stage.

This paper is organized into six sections. In Sect. 2, we provide a detailed description of the key Si RM model parameters. In Sect. 3, the measured inter-die statistical

 © 2023 The Japan Society of Applied Physics

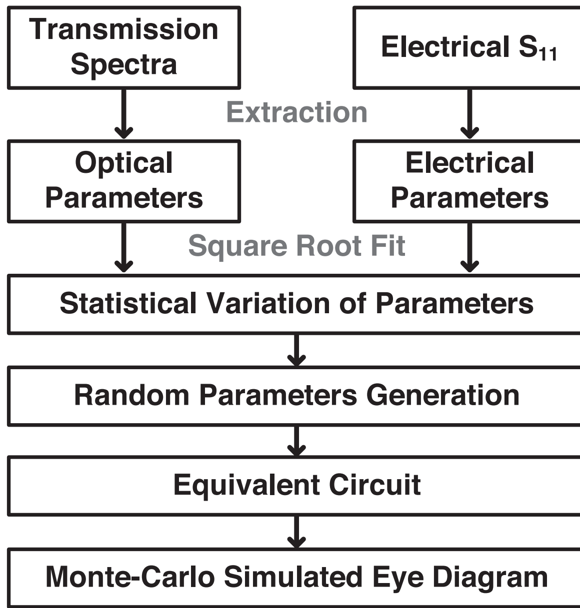

Fig. 1. Block diagram for Monte Carlo characterization scheme.

distributions of these model parameters are described, and the process of Monte Carlo analysis of 40-Gbps PAM-4 eye diagrams with correlated model parameters using the Si RM equivalent circuit in SPICE is explained. In Sect. 4, the Monte Carlo analysis results of PAM-4 eye diagram performance is analyzed. In Sect. 5, the proposed approach is extended to the Monte Carlo analysis of the entire Si electronic-photonic IC PAM-4 transmitter containing the RMs. Finally, Sect. 6 concludes the paper.

2. Model parameters

Figure 1 shows the block diagram of our Monte Carlo characterization scheme. First, the optical transmission spectra and the electrical reflection coefficients (S_{11}) of fabricated Si RM samples are measured at several different bias voltages. The RMs used for our investigation are fabricated by IHP's Si photonics technology from a multiple project wafer run. They have a nominally 12 μm ring radius and a 220 nm coupling gap between ring and bus waveguides, both of which are 500 nm wide and 220 nm thick rib waveguides with 100 nm slab thickness. The nominal peak carrier concentrations are 7×10^{17} cm^{-3} for the p-region and 3×10^{18} cm^{-3} for the n-region of the RM p-n junction.

The circles in Fig. 2(a) show the measured transmission spectra at several different bias voltages for one sample Si RM device used in our investigation. This measurement was performed at RT while the device was placed on a temperature-controlled stage. Although the temperature dependence can be included in the Monte Carlo characterization by using the temperature-aware model of the Si RM,[22] it has not been pursued in the present investigation. The Si RM transmission characteristics can be described with the equation given as[23]

$$T = \frac{P_{out}}{P_{in}} = \frac{\alpha^2 - 2\alpha\gamma\cos(\phi) + \gamma^2}{1 - 2\alpha\gamma\cos(\phi) + (\alpha\gamma)^2}, \quad (1)$$

where $\phi = 2\pi n_{eff} L/\lambda$ and L is the circumference of the ring. α is the field ratio after a round trip within the ring waveguide. γ is the through coupling coefficient in the directional coupler between the ring and bus waveguide of Si RMs, and n_{eff} is the effective refractive index at the resonance wavelength. By fitting the measured transmission spectrum to Eq. (1), numerical values for α, γ and n_{eff} can be determined for each bias voltage. The lines in Fig. 2(a) are the fitted transmission spectra using the extracted parameter values, which agree well with the measurement results. It is found γ has very little dependence on the bias voltage, and, therefore, a bias-voltage-independent γ value is used for our analysis.

The electrical characteristics of Si RMs are determined by the series resistance (R_s) and the junction capacitance (C_j) of the Si p-n junction within the Si RM. Their numerical values can be determined from the measured S_{11}.[24] The measured magnitude and phase of S_{11} of the same Si RM device at the different bias voltages are shown with circles in Figs. 2(b) and 2(c), respectively. By fitting these to the simulated S_{11} of an equivalent circuit representing the electrical characteristics of the Si RM,[24,25] the numerical values for R_s and C_j can be determined for each bias voltage. Lines in Figs. 2(b) and 2(c) show the well-matching fitting results. It is found that R_s has very little dependence on the bias voltage and, therefore, a bias-voltage-independent value for R_s is used for our analysis.

Figures 3(a)–3(c), respectively, show the extracted α, n_{eff} and C_j, values at different bias voltages for the sample Si RM device. Their bias-voltage dependence can be modeled with square root functions[26,27] given below:

$$\alpha = \alpha_{1/2}\sqrt{-V + 0.5} + \alpha_0, \quad (2)$$

$$n_{eff} = n_{1/2}\sqrt{-V + 0.5} + n_0, \quad (3)$$

$$C_j = 1/(C_{1/2}\sqrt{-V + 0.5} + C_0) \quad (4)$$

Numerical values for $\alpha_{1/2}$, α_0, $n_{1/2}$, n_0, $C_{1/2}$ and C_0 for the sample Si RM device are shown in Figs. 3(a)–3(c). In our investigation, these parameters, along with γ and R_s are used as model parameters for describing Si RM modulation characteristics.

3. Monte Carlo simulation

In order to obtain statistical distribution of 8 model parameters, the transmission spectra and the electrical S_{11} of nominally identical 48 Si RM devices (4 samples per die from 12 dies) are measured. Figures 4(a)–4(h) show the inter-die distribution of the model parameter values. Although they do not show perfect Gaussian distributions, most likely due to the limited number of devices measured, we fit the measurement results with the Gaussian distributions of model parameters as this provides a simple analysis. The mean and the standard deviation for each model parameter are shown in the figures, along with the least-mean-square Gaussian fitting results.

For accurate Monte Carlo characterization, the influence of statistical correlations among model parameters should be considered. For example, the parameters, $\alpha_{1/2}$, α_0, $n_{1/2}$ and n_0, are all influenced by the Si p-n junction structure within the Si RM, and, consequently, they have a certain amount of correlation. The cross-correlations among 8 model parameters can be determined from the measured statistical distributions and are shown in Table I. If the carrier concentration is higher, n_{eff} and R_s become smaller, while

© 2023 The Japan Society of Applied Physics

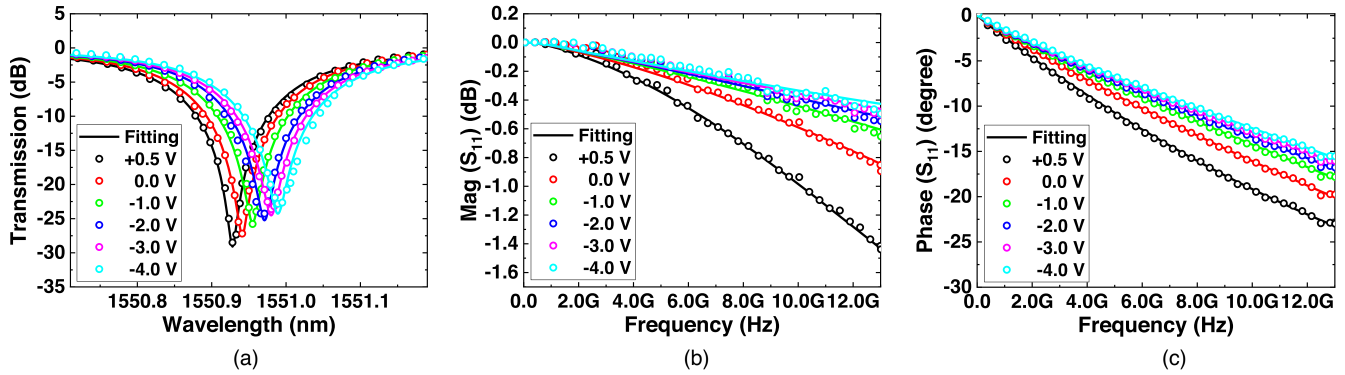

Fig. 2. (a) Measured and fitted Si RM transmission spectra, (b) magnitude and (c) phase of measured and fitted electrical S_{11} of Si RMs for different bias voltages.

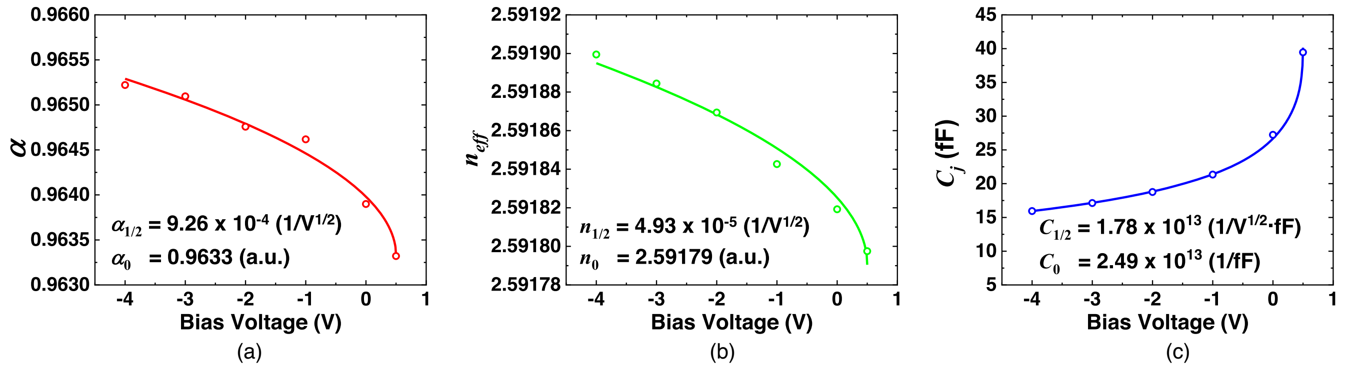

Fig. 3. Extracted model parameters (circles) for different bias voltages, (a) α, (b) n_{eff} and (c) C_{j}. Each solid curve is a square root fitting curve to parameterize bias-voltage dependency.

α and C_{j} become larger.[27,28] This is why n_0 and α_0 have strong negative cross-correlation, whereas n_0 and R_{s} have strong positive cross-correlation. Also, since $C_{1/2}$ and C_0 are in the denominator of C_{j} in Eq. (4), the cross-correlations between C_0 and R_{s}, $C_{1/2}$ and R_{s} have large positive values.

With the mean and the standard deviation for each model parameter and the cross-correlation among parameters, a set of correlated multi-variate Gaussian random numbers can be generated using the following relationship:[29,30)]

$$Y = \mu + A \cdot X, \tag{5}$$

where $Y = [\alpha_{1/2}, \alpha_0, \gamma, n_{1/2}, n_0, R_{\text{s}}, C_{1/2}, C_0]^{\text{T}}$ is the 8×1 column vector containing a set of random model parameters that can be used for Monte Carlo simulation, μ is the 8×1 column vector containing the mean value for each model parameter. X is the 8×1 column vector containing independent normally distributed random variables. For each run of Monte Carlo analysis, X is randomly produced, and modified so that the standard deviation of each parameter and cross-correlation among parameters are reflected by multiplying matrix A, which can be determined from the relationship

$$A \cdot A^T = C, \tag{6}$$

where C represents the covariance matrix of the model parameters whose element is given as

$$C_{x,y} = \rho_{xy}\sigma_x\sigma_y. \tag{7}$$

In the above equation, ρ_{xy} represents cross-correlation between parameters x and y, and σ_x and σ_y represent the standard deviation of parameters x and y, respectively. Once C is determined, A can be calculated from the Cholesky decomposition technique.[29,30] Applying Eqs. (5)–(7) to the measured model parameter statistics, the correlated model parameters set, Y, is repetitively determined for each run of Monte Carlo simulation.

For simulating the PAM-4 eye diagram, we use the Si RM equivalent circuit model shown in Fig. 5, which can accurately provide any large-signal transient response of Si RM modulation characteristics in SPICE.[25] In Fig. 5(a), Block A represents the Si RM electrical characteristics, and the RLC circuit in Block B shown in Fig. 5(b) represents the RM optical modulation characteristics. The circuit elements shown in Fig. 5(b) are used to model the behavior of the Si RM electro-optic modulation response and do not have any direct physical meaning. The equivalent circuit has the same transfer function for the modulation response of RMs, and the numerical values for the circuit elements are determined so that the resulting modulation characteristics are identical. From the coefficient comparison between the transfer function of RMs and that of the equivalent circuit, the numerical values of R_1, R_2, L and C are determined. The gain in the voltage-controlled voltage source, g, represents the transmission of the RM, which scales the simulated response of the equivalent circuit to the optical output power for each bias voltage as a type of voltage, V_{out}. Once the numerical values of the circuit in Fig. 5(b) are determined for each bias voltage as the model parameter relations in Ref. 25, the large-signal electro-optic response of RMs can be emulated for any input transient signal, V_{in}. From the correlated model parameter set produced by Eqs. (5)–(7), the

 © 2023 The Japan Society of Applied Physics

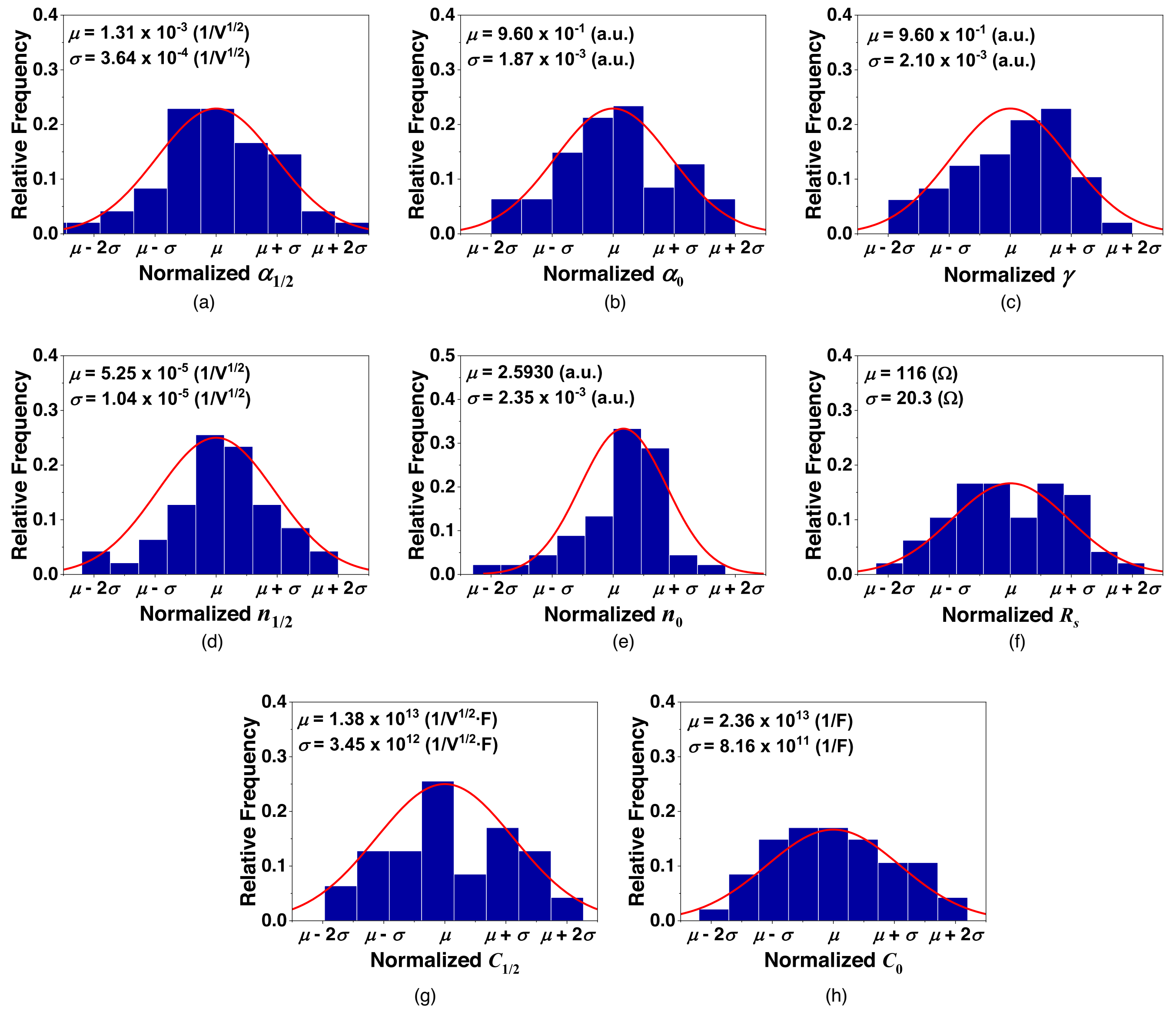

Fig. 4. Distributions of extracted model parameters (a) $\alpha_{1/2}$, (b) α_0, (c) γ, (d) $n_{1/2}$, (e) n_0, (f) R_s, (g) $C_{1/2}$ and (h) C_0.

Table I. Cross-correlations among 8 model parameters.

	$\alpha_{1/2}$	α_0	γ	$n_{1/2}$	n_0	R_s	$C_{1/2}$	C_0
$\alpha_{1/2}$	1.00	−0.30	0.25	0.06	0.13	0.03	0.00	0.07
α_0	−0.30	1.00	−0.24	0.37	−0.50	−0.11	−0.24	−0.20
γ	0.25	−0.24	1.00	−0.23	−0.08	−0.28	−0.06	−0.07
$n_{1/2}$	0.06	0.37	−0.23	1.00	−0.34	−0.35	−0.55	−0.60
n_0	0.13	−0.50	−0.08	−0.34	1.00	0.51	0.45	0.36
R_s	0.03	−0.11	−0.28	−0.35	0.51	1.00	0.81	0.75
$C_{1/2}$	0.00	−0.24	−0.06	−0.55	0.45	0.81	1.00	0.96
C_0	0.07	−0.20	−0.07	−0.60	0.36	0.75	0.96	1.00

numerical value for each circuit element in Figs. 5(a) and 5(b) can be generated for eye diagram simulation in SPICE. Specifically, the RC circuit in Block A is directly described by the model parameters R_s, $C_{1/2}$ and C_0. The values for R_1, R_2, L and C at a given bias voltage can be calculated using $\alpha_{1/2}$, α_0, γ, $n_{1/2}$ and n_0, with the relationship given in Ref. 25. Although the equivalent circuit in Fig. 5 contains circuit elements whose values depend on the bias voltage, they can be easily handled in SPICE, allowing very efficient and accurate simulation of nonlinear large-signal Si RM modulation characteristics. The use of this equivalent circuit is particularly advantageous since electrical and optical co-simulation of any transmitters containing Si RMs can be easily carried out within the standard IC design environment.[22,24,25,31] Furthermore, all the advanced design analysis capabilities available in SPICE can be easily applied.[18] Especially, the statistical variation of model parameters in this investigation is limited to an inter-die scale, but the statistical variation of model parameters is scalable in SPICE by defining the parameter variation as a mismatch and/or process.

Figure 6(a) shows the SPICE-simulated 40-Gbs PAM-4 eye diagram using the equivalent circuit for a sample Si RM

 © 2023 The Japan Society of Applied Physics

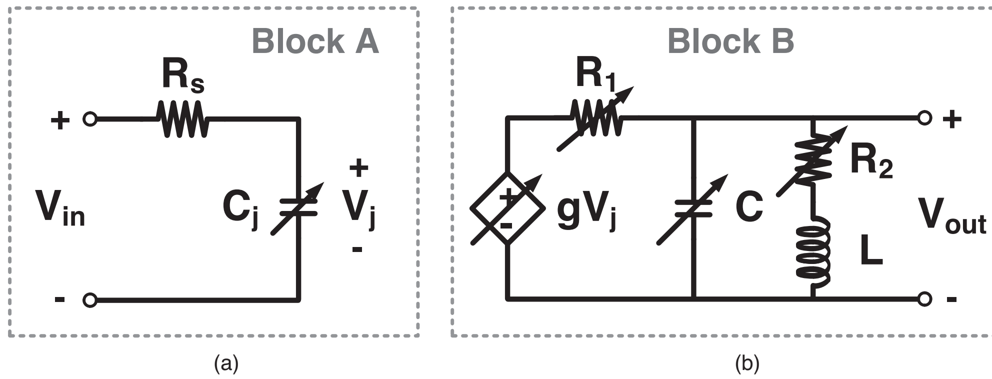

Fig. 5. Block diagram of equivalent circuit of Si RMs, (a) Block A for electrical components of RMs and (b) Block B for optical modulation characteristics of RMs.

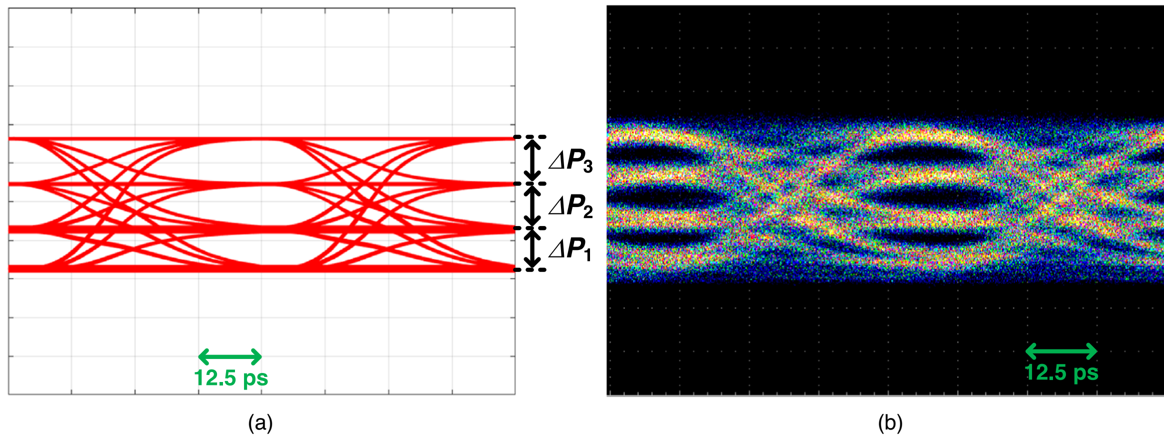

Fig. 6. (a) Simulated and (b) measured eye diagram of 40-Gbps PAM-4 modulated Si RM.

with the extracted model parameters whose values are given in Table II. The measured eye diagram for the same sample Si RM is also shown in Fig. 6(b), and their agreement is good. For the measurement, electrical PAM-4 signals (2.6 V_{pp}, −0.8 V_{dc}, PRBS $2^{31)}-1$) are supplied to the sample Si RM device. For PAM-4 modulation, the key performance metrics are OMA and RLM.[32–34] The OMA is defined to be an optical power difference between the bottom and the top level of PAM-4 signals, and the RLM is defined as

$$\mathrm{RLM}(\%) = 100 \times \frac{\min(\Delta P_1, \Delta P_2, \Delta P_3)}{\mathrm{avg}(\Delta P_1, \Delta P_2, \Delta P_3)}, \quad (8)$$

where ΔP_1, ΔP_2 and ΔP_3 denote the power difference of 4-level modulated signals, as shown in Fig. 6(a). For both simulation and measurement, the input wavelength is detuned from the resonance wavelength so that the RLM value is to be the highest value.

Table II. Measured model parameters for the simulation.

Parameter	Value	Unit
$\alpha_{1/2}$	0.926	10^{-3}/V$^{1/2}$
α_0	0.9633	a.u.
γ	0.9606	a.u.
$n_{1/2}$	4.93	10^{-5}/V$^{1/2}$
n_0	2.59179	a.u.
R_s	133.7	Ω
$C_{1/2}$	1.78	10^{13}/V$^{1/2}$F
C_0	2.49	10^{13}/F

4. Monte Carlo eye diagram analysis of RM

Figure 7 shows the Monte Carlo simulated eye diagram of 40-Gbps PAM-4 modulated Si RMs. The run number is 10,000. For each run, the input wavelength detuning is set so that the best RLM is achieved. In Fig. 7, a large amount of level fluctuation can be observed, indicating a concern for the yield of the investigated Si RMs due to process variation.

For further analysis, the RLM and the OMA are determined from each run of Monte Carlo simulated PAM-4 eye and their 2-D histogram is obtained as shown in Fig. 8. The mean values of RLM and OMA are 97.4% and 0.65, and the standard deviation values of RLM and OMA are 2.6% and 0.08, respectively. In order to verify the accuracy of the Monte Carlo simulation, we randomly selected 12 Si RMs and measured their 40-Gbps PAM-4 eye diagrams, and their OMA and RLM values are determined. These results are shown as black dots in Fig. 8. Table III shows the measured and the simulated values of RLM and OMA for the point A, B and C shown in Fig. 8 with the model parameters generated in the Monte Carlo simulation and the measurement. Also shown are the percentages of RMS error. If the target OMA and RLM are specified, the yield of Si RMs satisfying these specs can be predicted from this 2-D histogram. This should be of great help in further optimizing Si RM device structure and process steps with the yield consideration and also provide a useful design guide for Si RM driving circuits.

© 2023 The Japan Society of Applied Physics

Table III. The measured and simulated values of RLM, relative OMA and model parameters for the points A, B, and C.

Case	A		B		C		Unit
	Meas.	Sim.	Meas.	Sim.	Meas.	Sim.	
RLM	95.5	95.6	96.1	96.6	96.9	96.9	%
Relative OMA	0.603	0.597	0.638	0.619	0.708	0.727	a.u.
$\alpha_{1/2}$	1.19	1.22	1.97	1.9	1.21	1.19	$10^{-3}/V^{1/2}$
α_0	0.9628	0.9567	0.9597	0.9573	0.9563	0.9634	a.u.
γ	0.9614	0.9621	0.9606	0.9611	0.961	0.962	a.u.
$n_{1/2}$	5.57	5.48	5.07	5.08	5.09	5.18	$10^{-5}/V^{1/2}$
n_0	2.5886	2.5941	2.5923	2.5943	2.5944	2.5904	a.u.
R_s	92.9	89.9	122.1	121.9	126.9	124.8	Ω
$C_{1/2}$	0.99	1.01	1.87	1.82	1.73	1.68	$10^{13}/V^{1/2}F$
C_0	2.21	2.23	2.54	2.51	2.42	2.42	$10^{13}/F$
Parameters RMS error	1.75		1.55		1.33		%

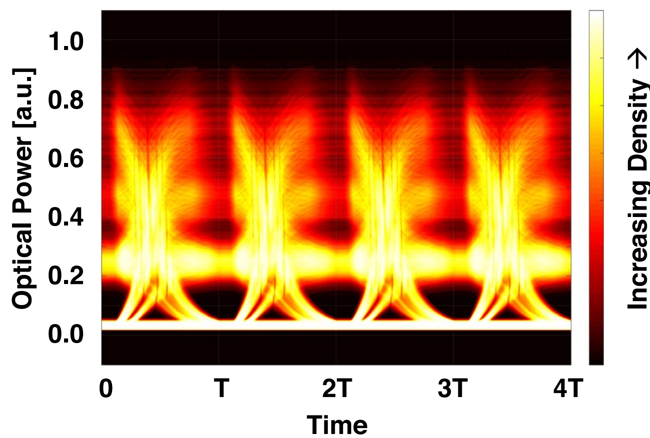

Fig. 7. The Monte Carlo simulated 40-Gbps PAM-4 eye diagram of Si RMs.

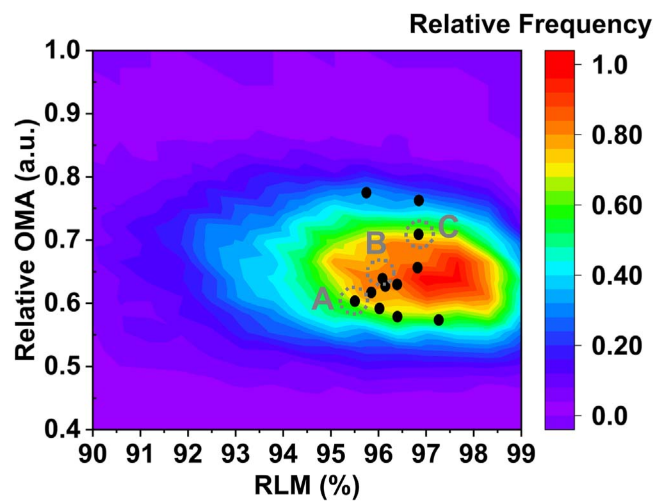

Fig. 8. 2-D histogram of Monte Carlo simulated OMA and RLM for 10,000 of run number when Si RM is modulated with 40-Gbps PAM-4 modulation signals. Black dots are the measured OMA and RLM values for 12 samples.

5. Monte Carlo eye diagram analysis of Si EPIC PAM-4 transmitter

The Si EPIC PAM-4 transmitter with an RM investigated in the paper is designed using IHP's Photonic BiCMOS technology.[35] Figure 9 shows the schematic diagram of the PAM-4 driver structure. It is composed of two parallel differential cascode amplifiers for the most significant bit (MSB) and least significant bit (LSB) signals. Since the process variations can greatly affect the performance of Si photonic components, their statistical distribution should be considered so that the performance margin of the entire EPIC can be carefully investigated for reliable and high-performance EPIC implementation in the design stage. The Monte Carlo simulation of driver IC can be easily performed based on the process statistical information provided by the chip manufacturer. With the Monte Carlo characterization of RMs described in Sects. 2–4, the eye diagram performance of RM can be co-simulated with the responses of driver electronics.

Figure 10(a) shows the Monte Carlo simulated 40-Gbps PAM-4 eye diagram of the RM driver electronics with the run number of 10,000 where the RLM of input signal to the RM driver is set to be 100%. The key performance metrics for the driver IC are driver output peak-to-peak voltage ($V_{peak\text{-}to\text{-}peak}$) and RLM, and their statistical variations are shown in Fig. 10(b). The resulting driver IC output signals are applied to the RM for the Monte Carlo simulation of the entire EPIC. Figure 10(c) shows the resulting eye diagram for the entire EPIC PAM-4 transmitter. These results clearly show the significant degradation in the EPIC eye quality due to the Si RM, indicating further development is needed for reducing process variation for Si RMs. The statistical variations of OMA and RLM for the EPIC transmitter are shown in Fig. 10(d). From this figure, it is possible to predict the yield of the EPIC transmitter OMA and RLM if their target values are given. This should provide very useful performance metrics for the EPIC in the design stage and will be of great help in optimizing the EPIC performance. Table IV provides the mean and standard deviation values for OMA and RLM determined from the Monte Carlo simulation. For comparison, the values for Si RM obtained from the data shown in Figs. 7 and 8 are also listed. The mean value of RLM for the EPIC is smaller than that of the RM since driver IC provides additional degradation. The mean

Table IV. Mean and standard deviation of Monte Carlo simulated Si EPIC PAM-4 transmitters.

	Case	μ	σ	Unit
RLM	RM	97.6	2.60	%
	Driver	97.8	0.53	%
	Driver + RM	92.9	2.64	%
$OMA/V_{peak\text{-}to\text{-}peak}$	RM	0.65	0.08	a.u.
	Driver	2.49	0.05	V
	Driver + RM	0.44	0.08	a.u.

© 2023 The Japan Society of Applied Physics

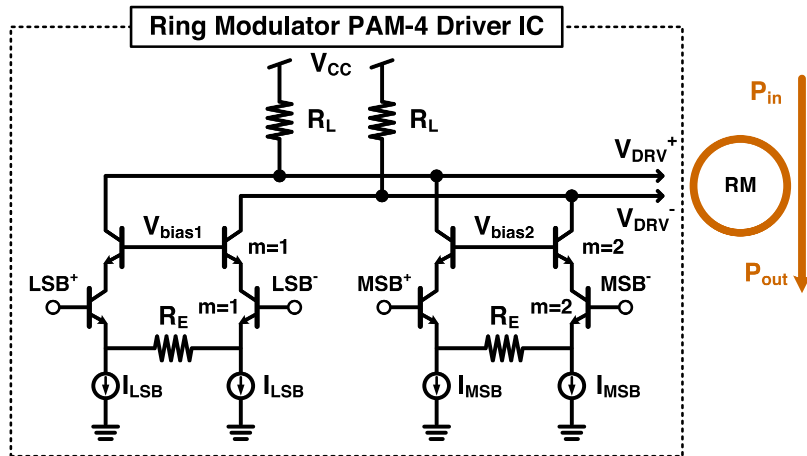

Fig. 9. Schematic diagram of Si EPIC PAM-4 transmitter containing RM.

Fig. 10. The Monte Carlo simulated 40-Gbps Si EPIC PAM-4 transmitters. (a) eye diagram and (b) 2-D histogram ($V_{peak\text{-}to\text{-}peak}$, RLM) of Monte Carlo simulated output of RM driver ICs. (c) eye diagram and (d) 2-D histogram of Monte Carlo simulated output of the entire Si EPIC PAM-4 transmitters. The run number for both cases is 10,000.

value of OMA for the EPIC is also smaller due to the degradation of the driver. However, the OMA and RLM standard deviation values are similar for both cases, since most of the contribution comes from the Si RM.

The device performance and yield can be further optimized with the proposed method. For example, if we want to enhance the 3-dB modulation bandwidth of the Si RM, the RM model parameters can be modified so that the target 3-dB bandwidth can be achieved. Then, the statistical variation of device performance can be re-simulated as previously described. Then, the RM device structure can be modified so that the desired model parameters can be obtained. Although not

 © 2023 The Japan Society of Applied Physics

pursued in this study, it is possible to carry out the device-level simulation of model parameters in consideration for the statistical variance in device structure, and the resulting variation in model parameters can be transformed into statistical variation in the circuit parameters of the equivalent circuit. In this way, the proposed method can provide the efficient simulation environment of Monte Carlo characterization of RMs for the yield-analysis-based feedback of the design.

6. Conclusion

The 40-Gbps PAM-4 eye diagram performance of Si RMs is Monte Carlo characterized in SPICE. From the measured transmission spectra and electrical S_{11} of Si RMs fabricated in a single wafer, the statistical distributions of 8 model parameters for Si RMs are obtained, which thenare converted to the correlated model parameter sets. With these model parameters and using the equivalent circuit for the Si RM, 40-Gbps PAM-4 eye diagrams of Si RMs are Monte Carlo simulated, and the 2-D histograms for OMA and RLM are produced and corroborated with the measurement. With this, the yield of Si RMs in PAM-4 modulation can be estimated. The proposed method can be expanded to a larger scale of statistical variation of parameters with the capability of SPICE. From this, the yield of the PAM-4 Si electronic-photonic transmitter can be estimated, as can how much contribution each of the electronic circuits and the RM makes. Our approach should be of great help for optimizing Si RM device structure, process steps, and the yield-aware design optimization of the entire Si electronic-photonic transmitter containing Si RMs and electronic circuits. This should assist in yield enhancement for optical I/O systems based on the Si RM.

Acknowledgments

This work was supported by the National Research Foundation of Korea (NRF) grant funded by the Korean government (MSIT) under Grant No. NRF2020R1A2C2015089 and the International Joint Research Grant by Yonsei Graduate School. The authors also thank the IC Design Education Center (IDEC) for EDA tool support.

ORCID iDs

Youngkwan Jo https://orcid.org/0000-0002-6351-7213

Yongjin Ji https://orcid.org/0009-0002-4619-0615

1) Y. Shen, X. Meng, Q. Cheng, S. Rumley, N. Abrams, A. Gazman, E. Manzhosov, M. S. Glick, and K. Bergman, J. Light. Technol. **37**, 245 (2019).
2) E. Luan, H. Shoman, D. M. Ratner, K. C. Cheung, and L. Chrostowski, Sensors **18**, 3519 (2018).
3) T. Claes, J. G. Molera, K. de Vos, E. Schacht, R. Baets, and P. Bienstman, IEEE Photonics J. **1**, 197 (2009).
4) D. Marpaung, C. Roeloffzen, R. Heideman, A. Leinse, S. Sales, and J. Capmany, Laser Photonics Rev. **7**, 506 (2013).
5) M. S. Rasras et al., J. Light. Technol. **27**, 2105 (2009).
6) X. Qiang et al., Nat. Photonics **12**, 534 (2018).
7) T. Rudolph, APL Photonics **2**, 030901 (2017).
8) B. J. Shastri, A. N. Tait, T. Ferreira de Lima, W. H. P. Pernice, H. Bhaskaran, C. D. Wright, and P. R. Prucnal, Nat. Photonics **15**, 102 (2021).
9) T. F. de Lima, H. T. Peng, A. N. Tait, M. A. Nahmias, H. B. Miller, B. J. Shastri, and P. R. Prucnal, J. Light. Technol. **37**, 1515 (2019).
10) S. K. Selvaraja, W. Bogaerts, P. Dumon, D. van Thourhout, and R. Baets, IEEE J. Sel. Top. Quantum Electron. **16**, 316 (2010).
11) L. Chrostowski, X. Wang, J. Flueckiger, Y. Wu, Y. Wang, and S. Talebi Fard, Opt. Fiber Commun. Conf. **37**, Th2A (2014).
12) N. Boynton, A. Pomerene, A. Starbuck, A. Lentine, and C. T. Derose, 2017 IEEE Optical Interconnects Conf., 2017, p. 11, 10.1109/OIC.2017.7965506.
13) S. R. Nassif, A. J. Strojwas, and S. W. Director, IEEE Trans. Comput.-Aided Des. Integr. Circuits Syst. **5**, 104 (1986).
14) C. Jacoboni and L. Reggiani, Rev. Mod. Phys. **55**, 645 (1983).
15) Z. Lu, J. Jhoja, J. Klein, X. Wang, A. Liu, J. Flueckiger, J. Pond, and L. Chrostowski, Opt. Express **25**, 9712 (2017).
16) W. Bogaerts, Y. Xing, and U. Khan, IEEE J. Sel. Top. Quantum Electron. **25**, 1 (2019).
17) K. M. Jabon et al., Opt. Fiber Commun. Conf., (2021). p. M3A. 1.
18) Y. Jo, Y. Ji, M. Kim, S. Lischke, C. Mai, L. Zimmermann, and W. Y. Choi, IEEE 17th Int. Conf. on Group IV Photonics (GFP), 2021, p. 1, 10.1109/GFP51802.2021.9673952.
19) G. Li, A. V Krishnamoorthy, I. Shubin, J. Yao, Y. Luo, H. Thacker, X. Zheng, K. Raj, and J. E. Cunningham, IEEE J. Sel. Top. Quantum Electron. **19**, 95 (2013).
20) M. Sakib, R. Kumar, C. Ma, D. Huang, X. Wu, G.-L. Su, and H. Rong, Optical Fiber Communication Conf. (OFC), 2022, p. M2D.4, 10.1364/OFC.2022.M2D.4.
21) S. Fathololoumi et al., J. Lightwave Technol. **39**, 1155 (2021).
22) M. Kim, Y. Jo, S. Lischke, C. Mai, L. Zimmermann, and W. Y. Choi, IEEE Photonics Technol. Lett. **33**, 947 (2021).
23) W. Bogaerts, P. de Heyn, T. van Vaerenbergh, K. de Vos, S. Kumar Selvaraja, T. Claes, P. Dumon, P. Bienstman, D. van Thourhout, and R. Baets, Laser Photonics Rev. **6**, 47 (2012).
24) M. Shin, Y. Ban, B. M. Yu, M. H. Kim, J. Rhim, L. Zimmermann, and W. Y. Choi, IEEE Trans. Electron Devices **64**, 1140 (2017).
25) M. Kim, M. Shin, M.-H. Kim, B.-M. Yu, Y. Kim, Y. Ban, S. Lischke, C. Mai, L. Zimmermann, and W.-Y. Choi, Photonics Res. **7**, 948 (2019).
26) E. Timurdogan, C. V Poulton, M. J. Byrd, and M. R. Watts, Nat. Photonics **11**, 200 (2017).
27) D. A. Neamen, *Semiconductor Physics and Devices: Basic Principles* (McGraw-hill, New York, 2012) 3rd ed., Chap. 7.
28) R. A. Soref and B. R. Bennett, IEEE J. Quantum Electron. **23**, 123 (1987).
29) K. S. Eshbaugh, IEEE Trans. Comput.-Aided Des. Integr. Circuits Syst. **11**, 1198 (1992).
30) CAD tool's user guide Synopsys, HSPICE User Guide "Basic Simulation and Analysis" Mountain View, CA, (2013).
31) M. Kim, M.-H. Kim, Y. Jo, H.-K. Kim, S. Lischke, C. Mai, L. Zimmermann, and W.-Y. Choi, Photonics Res. **9**, 507 (2021).
32) IEEE Standard, P802.3 bs 200 Gb/s and 400 Gb/s Ethernet Task Force. Jul. 1 (2020).
33) Standard OIF CEI-56G, Application Note. Jul. 1 (2020).
34) M. Kim, D. H. Kwon, D. W. Rho, and W. Y. Choi, IEEE Trans. Circuits Syst. II: Express Br. **68**, 908 (2021).
35) S. Lischke, D. Knoll, C. Mai, and L. Zimmermann, Proc. SPIE **11088**, 1108801 (2019).

© 2023 The Japan Society of Applied Physics